Engineering Hierarchical Porous Electrodes Integrated with Conformal Ultrathin Nanosheets for Achieving Rapid Kinetics in High-Power Microbatteries

Xin Chen [1,†], **Minjian Gong** [2,†], **Jiantao Li** [2,*], **Wei Yang** [1,*] **and Xu Xu** [2,3,*]

[1] School of Materials Science and Engineering, Wuhan University of Technology, Wuhan 430070, China; 331251@whut.edu.cn
[2] State Key Laboratory of Advanced Technology for Materials Synthesis and Processing, International School of Materials Science and Engineering, Wuhan University of Technology, Wuhan 430070, China; gongminjian@whut.edu.cn
[3] Zhongyu Feima New Material Technology Innovation Center (Zhengzhou) Co., Ltd., High Technology Industrial Development Zone, Zhengzhou 450001, China
[*] Correspondence: jiantao_work@126.com (J.L.); yangwei830@whut.edu.cn (W.Y.); xuxu@whut.edu.cn (X.X.)
[†] These authors contributed equally to this work.

Abstract: With the rapid development of the Internet of Things (IoT), there is an increasing demand for batteries with high energy and power densities. Three-dimensional microstructures present a promising approach for achieving high areal mass loading and an expanded electrochemical reaction surface. However, their high cost and complexity have hindered their widespread adoption. In this study, hierarchical porous electrodes integrated with conformal ultrathin nanosheets were fabricated to enhance reaction kinetics. The hierarchical porous skeleton provides a continuous pathway for electron transport and electrolyte diffusion, while the amorphous vanadium oxide (α-VO$_x$) nanosheets offer short ion diffusion channels and a large electrochemical surface area. Additionally, the internal space of the hierarchical structure accommodates substantial growth of the α-VO$_x$ nanosheets, thereby supporting high mass loading and preserving areal capacity. The resulting hierarchical electrode structure demonstrates a high energy density of 0.49 mAh cm^{-2} at 1 mA cm^{-2} and an ultrahigh power density of 410 mW cm^{-2} at 250 mA cm^{-2}. The assembled microbattery, using lithium metal as the anode, is encapsulated with a novel packaging process. This microbattery can power an electronic clock for up to 18 h on a single charge, retaining 75% of its initial capacity after 180 cycles.

Keywords: keyword hierarchical porous; ultrahigh power density; micro lithium battery

1. Introduction

With the rapid development of mass consumer electronics and the Internet of Things (IoT) [1–3], there is an increasing demand for energy storage devices with higher performance, particularly in terms of energy and power density [4,5]. As electronic devices continue to miniaturize, they rely heavily on small button batteries. Conventional button batteries, which use densely stacked active materials for high areal energy density, suffer from limited electron transport and ion diffusion paths, resulting in low output currents that fail to meet the power requirements of small microelectronic devices. Consequently, the development of microbatteries with both high energy and power densities has become urgent [6]. Meanwhile, there is growing interest in aqueous microbatteries [7–9], particularly those based on zinc electrodes, such as Mn-Zn [10,11], I$_2$-Zn [12], and PBA-Zn [13] batteries.

While these devices can deliver relatively high power densities, their limited operating voltage window leads to low energy densities. As a result, micro lithium batteries, which offer both a high voltage window and high energy density, are emerging as the preferred choice.

Researchers are currently employing strategies such as anode-free [14,15] designs and 3D printing [16,17] to maximize energy density. However, achieving high power densities at high active mass loadings [18] remains a significant challenge. The simultaneous attainment of high energy and power densities in conventional batteries is difficult, as increased material loading reduces the contact area between the electrode material and the electrolyte, increases ion transport distances, and disrupts electron conduction paths. To address this, strategies such as gradient [19,20] and three-dimensional electrode structures [21–24] are often used to enhance the power density. However, the 3D structuring of electrodes is frequently associated with high cost and complexity. Therefore, developing low-cost, low-complexity electrode fabrication methods is essential for advancing microbatteries. Electrochemical deposition, which is highly controllable, cost-effective, environmentally friendly, and easy to implement, is commonly used to prepare materials such as transition metal oxides and hydroxides [25].

In this work, a hierarchical porous electrode with ultrathin α-VO$_x$ nanosheets was fabricated. The hierarchical porous current collector was prepared using a hydrogen templating method on nickel foam, followed by the conformal construction of ultrathin α-VO$_x$ nanosheets within this framework to create high-performance electrodes. This hierarchical structure provides ample space for the growth of active materials, continuous pathways for electron conduction, and efficient electrolyte diffusion. Additionally, the high specific surface area ensures a large electrochemical interface, while the ultrathin nanosheets offer short ion diffusion paths. The resulting electrode demonstrates a high energy density of 0.49 mAh cm^{-2} and a power density of 410 mW cm^{-2}. Furthermore, a lithium microbattery based on this high-performance electrode was developed, incorporating a novel packaging strategy that achieves a cycle life of 180 cycles and powers an electronic clock for over 18 h on a single charge.

2. Materials and Methods

Chemicals: Nickel sulfate hexahydrate (NiSO$_4$·6H$_2$O), ammonium sulfate ((NH$_4$)$_2$SO$_4$), Vanadium (IV) oxide sulfate hydrate (VOSO$_4$·xH$_2$O), sodium acetate (CH$_3$COONa). All the chemicals were used directly after purchase.

Fabrication of 3D hierarchical porous current collector: A 3D hierarchical porous current collector was fabricated on commercial nickel foam using the electrodeposition process to construct an electrode current collector. First, an electrolyte with a concentration of 0.1 M NiSO$_4$ and 0.75 M (NH$_4$)$_2$SO$_4$ was configured. A two-electrode electrodeposition process was carried out using a DC-regulated power supply. A $2.5 \times 0.5 \times 0.01$ cm^3 nickel foam was used as the working electrode and a Pt foil was used as the counter electrode. Then, the typical electrodeposition was performed with a constant current of 1–3 mA cm^{-2} for 1–3 min. The 3D hierarchical porous current collector was rinsed with deionized (DI) water, followed by drying at 80 °C for 30 min.

Active materials deposition: Once the porous nickel was fabricated on the nickel foam to form a hierarchical porous current collector structure, the VO$_x$ cathode material was deposited on the current collector by cyclic voltammetry. Among them, a 3D hierarchical porous current collector, Pt foil, and a saturated Ag/AgCl electrode were used as the working electrode, counter electrode, and reference electrode, respectively. The electrodeposition process was carried out at a sweep rate of 50mV s^{-1} in the operating voltage range of

0–1.2 V for 300 cycles. The completed hierarchical porous VO$_x$ electrode was rinsed with DI water, followed by drying at 80 °C for 6 h.

Assembly of HP-VO$_x$//Li MB: The HP-VO$_x$ microelectrodes and lithium–copper composite tape microelectrodes were affixed to commercial nano-adhesives, and the microelectrodes were covered with a box-type nano-adhesive. Subsequently, the nano-adhesive fit should be coated with TB-6201 UV curing adhesive. Once the light-curing adhesive has undergone the curing process, the electrolyte should be added to the electrode. The PE film should then be pasted on the top side of the frame-type nano-adhesive. Finally, the light-curing adhesive should be used to coat the PE film and nano-adhesive fit.

Material characterization and electrochemical testing: The coin-type cells with hierarchical porous electrodes as positive electrodes and lithium metal as negative electrodes were investigated using a 2500 separator (Celgard, NC, USA) and 1 M LiTFSI in DME—DOL = 1:1 Vol%—with 1% LiNO$_3$ as electrolyte. Scanning electron microscopy (SEM) images were obtained with a JEOL JSM-7100F SEM (JEOL Ltd., Tokyo, Japan) at an acceleration voltage of 15.0 kV. The microscope pictures were taken using a light microscope with a 20× objective lens. Energy dispersive X-ray spectroscopy (EDS) results were recorded by an Oxford IE250 system (Oxford Instruments Co., Oxford, UK). X-ray photoelectron spectroscopy (XPS) results were recorded by the AXIS SUPRA (Shimadzu Group Co., Kyoto, Japan). Transmission electron microscope (TEM) results were obtained with a JEM-1400Plus (JEOL Ltd., Tokyo, Japan). High-resolution transmission electron microscopy (HRTEM) results were obtained with a JEM-2100F (JEOL Ltd., Tokyo, Japan). Atomic force microscope (AFM) (Dimension ICON-IR, Bruker Ltd., Karlsruhe, Germany) results were obtained with a Dimension ICON-IR. X-ray diffractometer result (XRD) was obtained by the D8 Discover (Bruker Ltd., Karlsruhe, Germany). Constant current charge/discharge curve results were tested through the Neware BTS83 battery test system (Neware Ltd., Shenzhen, China) and the long cycle result was tested by the Land T2001A battery testing station (LAND Ltd., Wuhan, China). Cyclic voltammetry curve (CV) results were tested within a voltage window of 1.8–3.8 V and the electrochemical impedance spectroscopy (EIS) results were measured in a frequency range of 0.01–100,000 Hz by the CHI760D. ECSA results were obtained from the electrochemical workstation CHI760D (Chenhua Ltd., Shanghai, China). GITT results were conducted on Land T2001A battery testing stations with a voltage window range of 1.8–3.8 V. The current pulse of 1 mA cm^{-2} for 1 min and the following relaxation for 30 min were applied in the GITT test.

3. Results and Discussion

As schematically illustrated in Figure 1, hierarchical porous electrodes were fabricated via electrodeposition. The hierarchical porous current collector was first created by introducing secondary pores into commercial nickel foam using the hydrogen bubble templating method. Subsequently, α-VO$_x$ nanosheets were deposited onto the hierarchical porous current collector through an electrodeposition process (Figure 1a,b). For microbattery packaging with a lithium metal anode, the organic electrolyte leakage, which is closely linked to battery performance and safety, has been a persistent issue. To address this, we employed a reproducible, highly efficient, and cost-effective double-stacked encapsulation process. This method ensures that the electrolyte remains within the interdigital electrodes over extended periods (Figure 1c). As shown in Figure 1d, excellent electronic conductivity is provided by a continuous structure composed of nickel foam and porous nickel, and a large reactive area and short ion-transfer path are realized by ultrathin nanosheets, which ingeniously achieve excellent electron-ion bicontinuity.
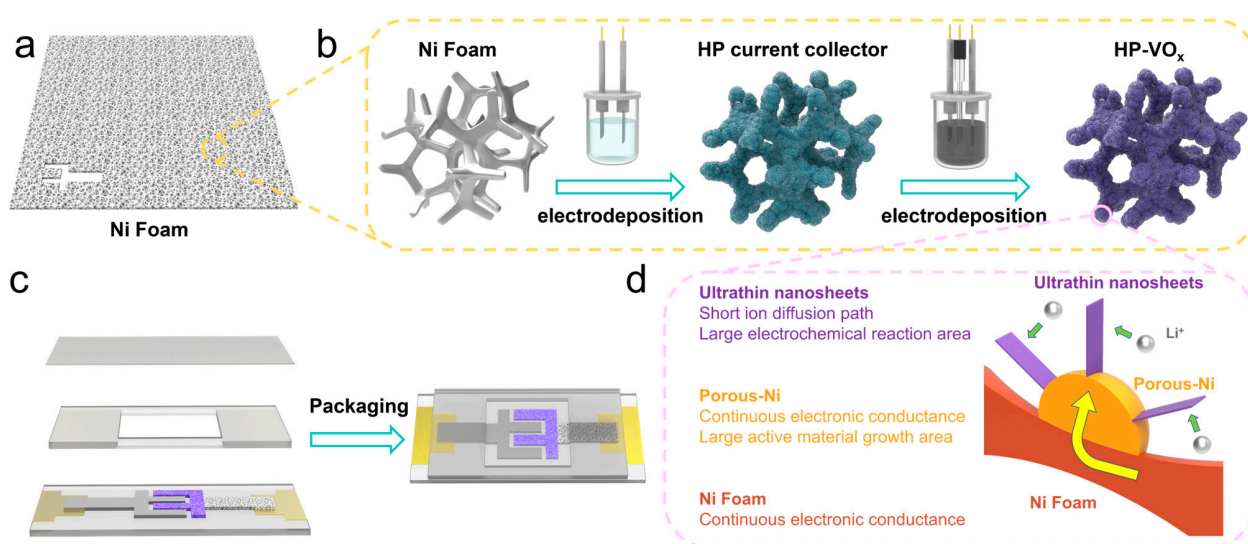
Figure 1. Fabrication process of hierarchical porous electrodes. (**a**) The diagram of the interdigital microelectrode from the commercial Ni foam. (**b**) Fabrication of hierarchical porous electrodes. (**c**) Package for lithium microbattery. (**d**) Reaction mechanism diagram of microelectrode.

Suitable parameters for preparing hierarchical porous electrodes were determined based on the results shown in Figures S1–S5 (Supporting Information). A microscope image of the hierarchical porous current collector (Figure S6a, Supporting Information) reveals that the original pores of the nickel foam remain intact, with secondary pores uniformly distributed throughout the structure. Electrochemical active areas of the nickel foam and hierarchical porous current collectors were subsequently evaluated (Figure S7, Supporting Information), showing that the hierarchical porous current collector has an active area six times larger than the original. This enhancement enables higher active material loading and promotes efficient ion and electron transport. Given the significant influence of electrodeposition solution concentration on the structure and properties of the electrodes, and consequently on their ion and electron transport capabilities, tests were conducted at various concentrations. Electrodeposition solutions of 20, 40, 50, 75, and 100 mM were prepared and applied via cyclic voltammetry over 300 cycles, with a voltage range of 0–1.2 V and a sweep rate of 50 mV s^{-1} (denoted as HP-VO$_x$-20, 40, 50, 75, and 100, respectively). Additionally, α-VO$_x$ was directly electrodeposited onto flat nickel foam, designated as P-VO$_x$-50. Comparative SEM images of these electrodes are provided in the Supporting Information (Figures S8–S12).

The morphology of the HP-VO$_x$-50 electrode was analyzed using scanning electron microscopy (SEM) (Figure 2a and Figure S13, Supporting Information). Unlike the material structure of nickel foil, [26] the active material and nickel particles feature large pores distributed across the nickel foam's cross-structure. Optical microscopy (Figure S6b, Supporting Information) confirms that the primary and secondary pores of the nickel foam retain their original structure, indicating the successful construction of α-VO$_x$ nanosheets through electrodeposition. Energy-dispersive spectroscopy (EDS) mapping (Figure 2b) demonstrates the uniform distribution of V and O elements, verifying consistent α-VO$_x$ loading across the electrode. Similar results from other electrodes (Figures S14–S18, Supporting Information) further confirm the homogeneity of α-VO$_x$ during electrodeposition. This hierarchical structure enhances surface area and active sites, facilitating the growth of active materials and providing ion transport pathways. Atomic force microscopy (AFM) results (Figure 2c) reveal that the electrodeposited nanosheets are 5–7 nm thick, supporting efficient ion diffusion. Additionally, the HP-VO$_x$-50 electrode surface exhibits greater roughness (Figure S19a, Supporting Information) than the standard hierarchical porous electrode

(Figure S19b, Supporting Information). Transmission electron microscopy (TEM) and high-resolution TEM (HRTEM) further characterize the α-VO$_x$ nanosheets. Figure 2d shows that individual nanosheets are 6–8 μm long and about 500–800 nm wide. The absence of clear lattice fringes in the HRTEM image (Figure 2e) confirms the amorphous nature of the α-VO$_x$ nanosheets, which provide abundant reaction sites. EDS results (Figure 2f) reinforce the uniform distribution of V and O elements. X-ray diffraction (XRD) analysis (Figure 2g) reveals peaks at $2\theta = 44°$, $51°$, and $76°$, corresponding to the nickel substrate, with no visible crystalline peaks, consistent with the amorphous nature observed in Figure 2e. This structural feature ensures efficient ion transport and ample electrochemical reaction interfaces. X-ray photoelectron spectroscopy (XPS) characterization (Figure 2h,i) of the HP-VO$_x$-50 electrode identifies V $2p_{3/2}$ peaks at 517.7 eV and 516.2 eV, corresponding to V^{5+} and V^{4+}, respectively, indicating the presence of high-valence vanadium species. Raman spectroscopy (Figure S20, Supporting Information) exhibits distinct peaks at 153, 262, and 700 cm^{-1}. The peak at 153 cm^{-1} is attributed to backbone bending vibrations: 262 cm^{-1} to O-V-O bond bending vibrations, Ref. [27], and 700 cm^{-1} to V-O bond stretching vibrations, Ref. [28], confirming the material as vanadium oxide.
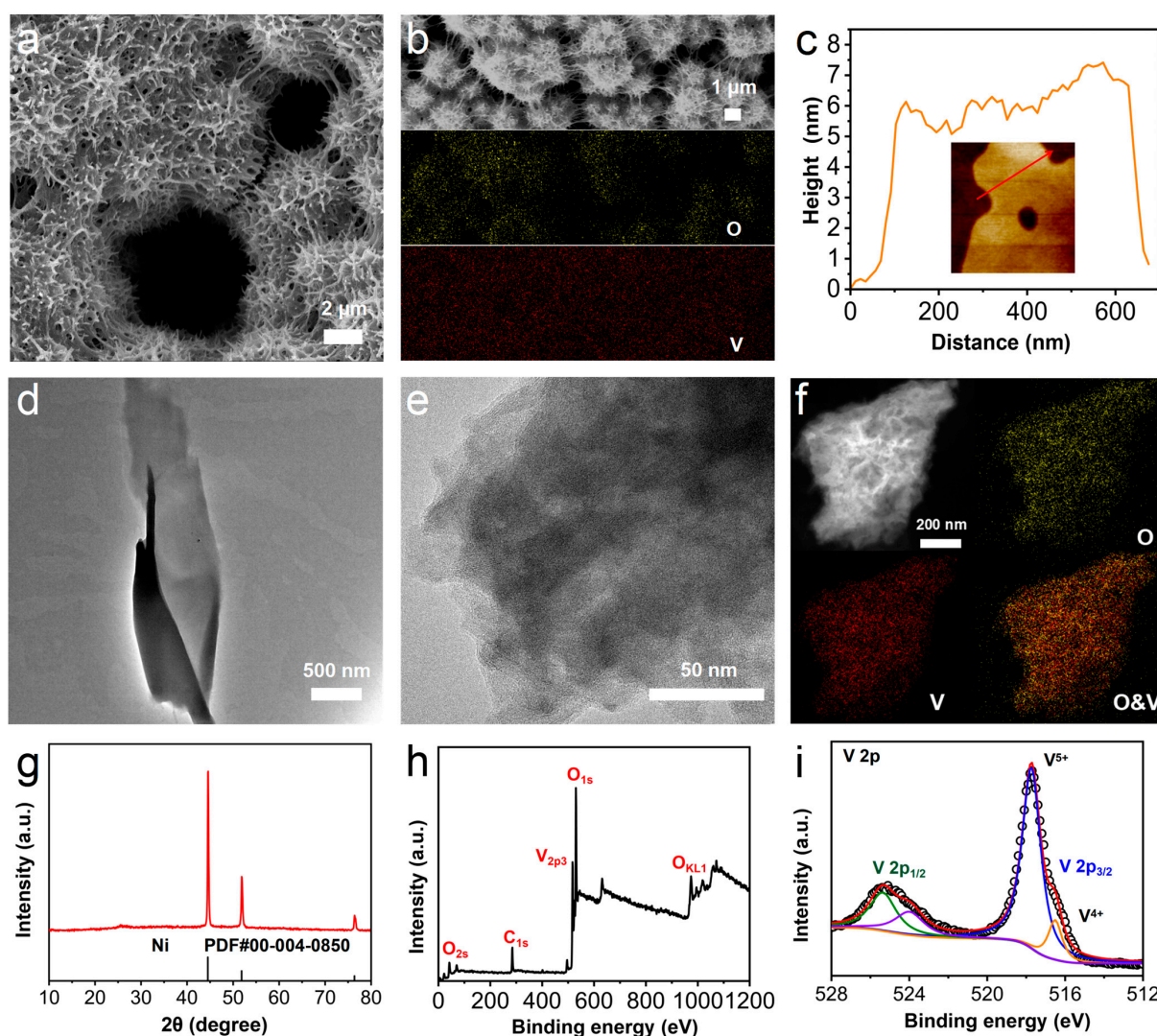

Figure 2. Structural characterization of hierarchical porous electrodes. (**a**) SEM images of HP-VO$_x$-50 electrodes. (**b**) EDS mapping images of V and O elements of HP-VO$_x$-50. (**c**) AFM image of HP-VO$_x$-50 electrode. (**d**) TEM image of VO$_x$. (**e**) HRTEM image of VO$_x$. (**f**) EDS mapping images of V and O elements of VO$_x$. (**g**) XRD image of HP-VO$_x$-50 electrode. (**h**) XPS full spectrum and (**i**) V 2p spectrum of HP-VO$_x$-50 electrode.

Coin-type batteries were assembled using these electrodes as cathodes to evaluate the electrochemical performance of the hierarchical porous electrodes. Figure 3a presents the galvanostatic charge/discharge (GCD) curves of the HP-VO$_x$-20, 40, 50, 75, and 100 electrodes at a current density of 1 mA cm^{-2}. As the electrodeposition solution concentration increases (20–100 mM), the energy density of the electrodes exhibits a general upward trend, maintaining a consistent voltage plateau (2.3–3.0 V), which indicates sufficient specific surface area within the hierarchical porous structure to accommodate the active material. Figure 3b displays the capacities of these electrodes at different current densities. At 1 mA cm^{-2}, the capacities are 0.05, 0.21, 0.49, 0.40, and 1.12 mAh cm^{-2} for the HP-VO$_x$-20, 40, 50, 75, and 100 electrodes, respectively. However, at higher current densities (10 mA cm^{-2}), the capacities decrease to 0.03, 0.10, 0.37, 0.25, and 0.39 mAh cm^{-2}, respectively. The HP-VO$_x$-75 and HP-VO$_x$-100 electrodes exhibit significant capacity loss due to excess VO$_x$ material clogging the porous structure, which impedes ion diffusion. Notably, the HP-VO$_x$-50 electrode retains an energy density of 0.22 mAh cm^{-2} even at 50 mA cm^{-2}, demonstrating its superior ion transport capabilities. Figure 3c shows the Ragone plot, where it is evident that while the HP-VO$_x$-75 and HP-VO$_x$-100 electrodes achieve high energy densities, their power densities are poor. Conversely, the HP-VO$_x$-50 electrode exhibits an optimal balance of energy and power densities, achieving a high energy density of 1.27 mWh cm^{-2} at 1 mA cm^{-2} and an ultrahigh power density of 410 mW cm^{-2} at 250 mA cm^{-2}. Figure 3d highlights the GCD curves of the HP-VO$_x$-50 electrode across a current density range of 1–50 mA cm^{-2} with a voltage window of 1.8–3.8 V. These curves maintain a stable voltage plateau and high Coulombic efficiency, even as the current density increases. GCD curves for the other electrodes under varying current densities are included in Figures S21–S24 (Supporting Information). Figure 3e compares the performance of the HP-VO$_x$-50 electrode with the P-VO$_x$-50 electrode, which lacks secondary pore structures. The P-VO$_x$-50 electrode shows a substantial decrease in energy density, attributed to insufficient active sites for VO$_x$ growth and an uneven material stacking structure, leading to pronounced capacity decay (Figure S25, Supporting Information). The HP-VO$_x$-50 electrode, on the other hand, benefits from its hierarchical structure, maintaining higher energy density and improved performance. The cycling performance of the HP-VO$_x$-50 electrode was tested at a high current density of 20 mA cm^{-2} (Figure 3f,g). Remarkably, the electrode retains nearly 100% of its capacity after 700 cycles, demonstrating excellent long-term stability. The capacity values remain consistent with those observed in Figure 3d. Finally, the Ragone plot in Figure 3h compares the energy and power densities of the HP-VO$_x$-50 electrode with those of previously reported micro lithium batteries [29–33]. This comparison underscores the superior performance of the HP-VO$_x$-50 electrode in balancing high energy and power densities. In addition, the HP-VO$_x$-50 electrode was characterized after cycling. The XRD and SEM results shown in Figures S26 and S27 (Supporting Information) illustrate that the electrode maintains the hierarchical porous structure of amorphous vanadium oxides after long cycling. Similarly, the EDS results of Figure S28 demonstrate the uniform distribution of the V and O elements.
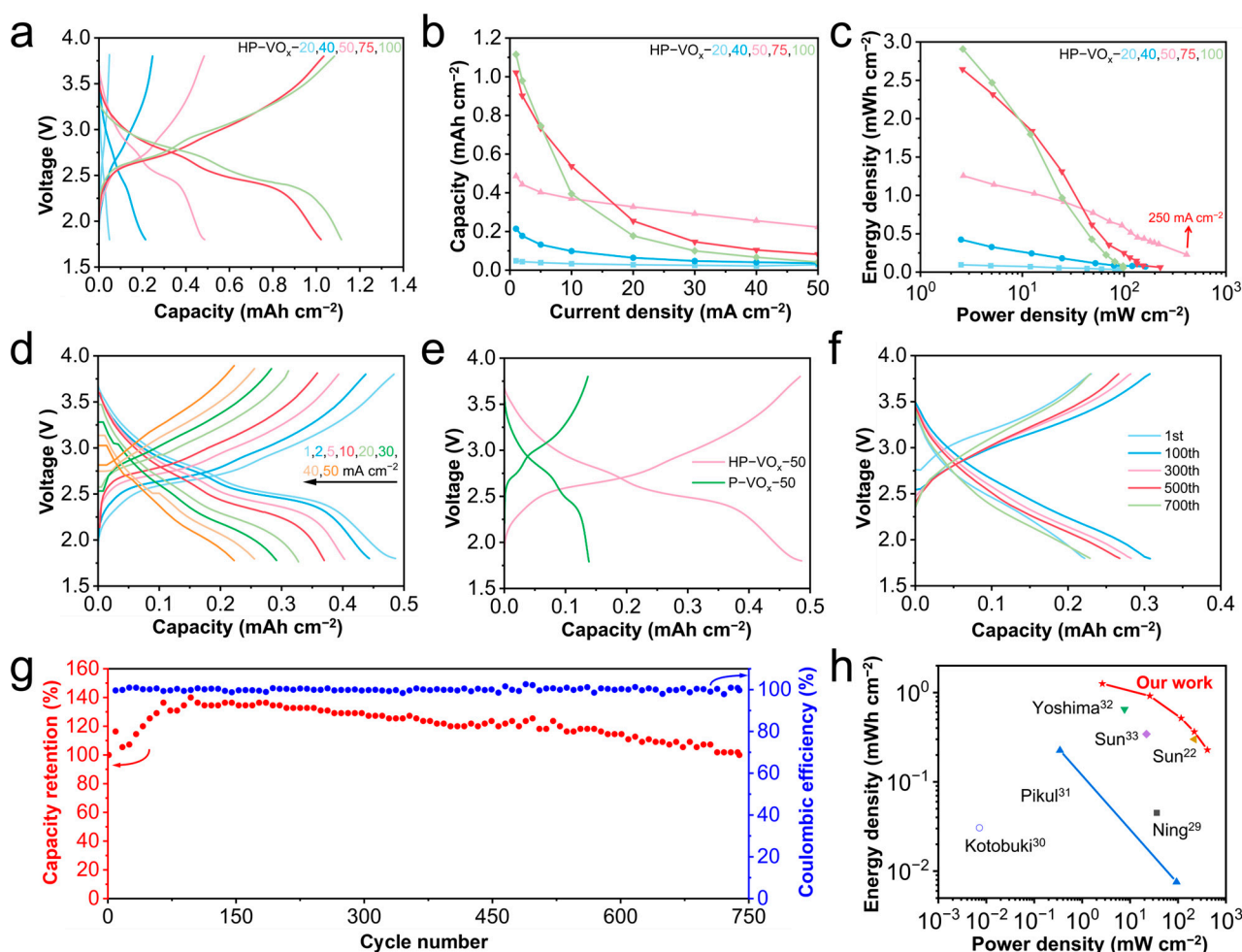
Figure 3. Electrochemical properties of HP-VO$_x$-20, 40, 50, 75, 100, and P-VO$_x$-50 electrodes. (**a**) GCD curves and (**b**) capacities at various current densities of different HP-VO$_x$ electrodes. (**c**) Ragone plot of each electrode. (**d**) GCD curves of HP-VO$_x$-50 electrode at various current densities. (**e**) Capacity comparison of HP-VO$_x$-50 and P-VO$_x$-50 electrodes. (**f**) Comparison of the capacity of HP-VO$_x$-50 electrode at different number of cycles. (**g**) Cycling performance of HP-VO$_x$-50 electrode. (**h**) Ragone plot showing the performance of our battery and other reported batteries.

To evaluate the electrochemical behavior of the HP-VO$_x$-50 electrode and its ability to maintain high power density, cyclic voltammetry (CV) tests were conducted at sweep rates of 1 to 5 mV s^{-1}, with results shown in Figure 4a. The CV curves remained nearly identical across the varying sweep rates, indicating stable electrochemical performance. Two reduction peaks at 2.4 V and 2.8 V in the cathodic sweep at 1 mV s^{-1} were observed, consistent with the GCD results. To further investigate the reaction kinetics and charge storage mechanisms of the HP-VO$_x$-50 electrode, a power–law relationship between the peak current (*i*) and sweep rate (*v*) was analyzed, as shown in Equation (1) [34]:

$$i = av^b \tag{1}$$

where *a* and *b* are constants related to the peak current and sweep rate. The value of *b* is typically between 0.5 and 1, representing diffusion-controlled and capacitance-controlled behavior, respectively. The log(*i*)-log(*v*) plots in Figure 4b were used to calculate the *b*-values for the oxidation and reduction peaks of the HP-VO$_x$-50 electrode, yielding values of 0.87 and 0.65, respectively. This indicates a combination of diffusion-controlled and capacitive behavior. Figure 4c further illustrates that as the sweep rate increases, surface capacitive behavior becomes more pronounced, with a *b*-value of 0.73 for both the oxidation

and reduction peaks. To quantify the contributions of diffusion-controlled and capacitance-controlled behaviors, the total current response at a given potential was separated into diffusion-controlled ($k_1 v$) and capacitive ($k_2 v^{1/2}$) components, as shown in Equation (2) [35]:

$$i = k_1 v + k_2 v^{\frac{1}{2}} \tag{2}$$
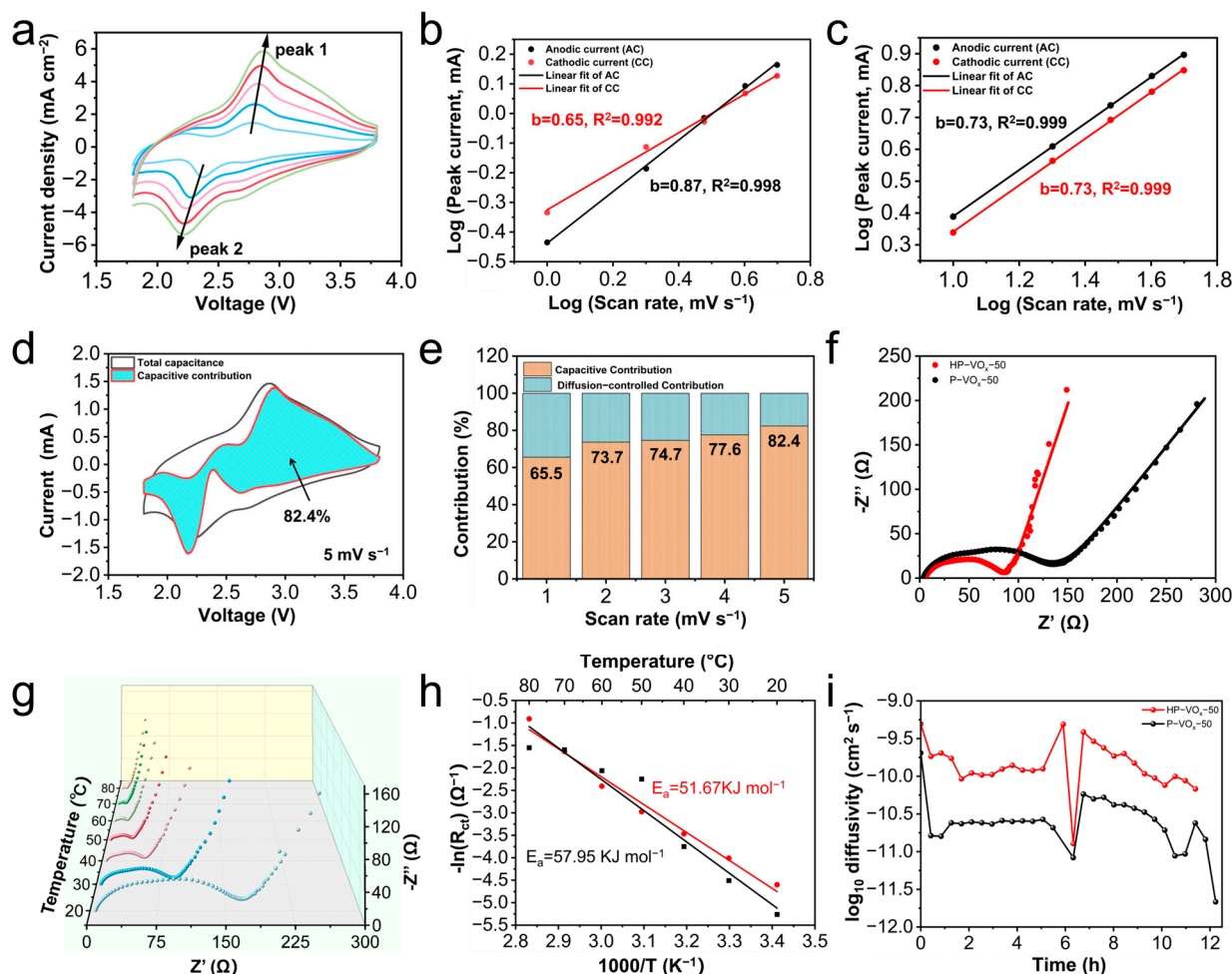

Figure 4. Electrochemical properties of HP-VO$_x$-50 electrode. (**a**) CV curves at sweep rates of HP-VO$_x$-50 electrode. (**b**) Determination of the b-value of the redox peaks by evaluating the relationship between the peak current and the sweep rates of the HP-VO$_x$-50 electrode from 1 to 5 mV s^{-1} and (**c**) from 10 to 50 mV s^{-1}. (**d**) The cyan region from 1.8 to 3.8V shows capacitive contribution. (**e**) Separations of capacitive and diffusion-controlled contribution at different sweep rates for HP-VO$_x$-50 electrode. (**f**) EIS curves for HP-VO$_x$-50 and P-VO$_x$-50 electrodes. (**g**) 3D EIS plots of HP-VO$_x$-50 electrode at different temperatures. (**h**) Fitting and activation energy plots of $-ln(R_{ct})$ at about $1000/T$ for HP-VO$_x$-50 electrode. (**i**) Comparison of Li$^+$ diffusion rates for HP-VO$_x$-50 and P-VO$_x$-50 electrodes.

Figure 4d presents the contributions of these behaviors for the HP-VO$_x$-50 electrode at a sweep rate of 5 mV s^{-1}, where the capacitive contribution (cyan region) accounts for 82.4% of the total performance. Additionally, the capacitive contribution at various sweep rates (1–4 mV s^{-1}) is shown in Figure S29 (Supporting Information), with values of 65.5%, 73.7%, 74.7%, and 77.6%, respectively. As shown in Figure 4e, the capacitive contribution increases steadily with the sweep rate, reaching 82.4% at 5 mV s^{-1}, suggesting that the electrode predominantly undergoes surface capacitive reactions with faster reaction kinetics at higher sweep rates.

To investigate the impact of the secondary structure on the electrochemical reaction mechanism of the electrode, we performed electrochemical impedance spectroscopy (EIS) on both the HP-VO$_x$-50 and P-VO$_x$-50 electrodes, with results shown in Figure 4f. The impedance of the electrode with the hierarchical porous structure is significantly lower, indicating improved ion and electron transport.

Next, the electrochemical impedance of the HP-VO$_x$-50 electrode was evaluated at varying temperatures, with 3D impedance spectra between 20 and 80 °C shown in Figure 4g. The EIS curve remains consistent across the temperature range, suggesting that the electrode maintains stable electrochemical performance at elevated temperatures. In contrast, the P-VO$_x$-50 electrode exhibits relatively higher impedance, as shown in Figure S30 (Supporting Information). Figures S31 and S32 (Supporting Information) further confirm that the charge transfer resistance (R_{ct}) of P-VO$_x$-50 is higher at all temperatures, suggesting that hierarchical porous electrodes with secondary pore structures provide more electrochemical reaction surface area, significantly enhancing reaction kinetics. Finally, the reaction activation energy was calculated using the Arrhenius equation, as detailed below [36]:

$$lnk = \frac{E_a}{RT} + lnA \qquad (3)$$

where A is the prefinger factor, T is the thermodynamic temperature, R is the gas constant, and E_a is the activation energy. Figure 4h shows the linear fit of $-ln(R_{ct})$-1000/T, which further yields a reaction activation energy of 51.67 kJ mol^{-1} for HP-VO$_x$-50 compared to 57.95 kJ mol^{-1} for P-VO$_x$-50, suggesting that the hierarchical structure can accelerate the reaction kinetics to some extent. Furthermore, the galvanostatic intermittent titration technique was employed to determine the Li$^+$ diffusion coefficient in HP-VO$_x$-50 and P-VO$_x$-50 electrodes, utilizing the following equation [37]:

$$D = \frac{4}{\tau\pi}\left(\frac{m_B V_m}{M_B S}\right)^2\left(\frac{\Delta E_s}{\Delta E_t}\right)^2\left(\tau \ll \frac{L^2}{D}\right) \qquad (4)$$

where τ is the time of applying constant current, m_B is the mass of the active substance (g), V_m is the molar volume of the sample (cm^3 mol^{-1}), M_B is the relative molecular mass of the material (g mol^{-1}), S is the contact area of the electrode/electrolyte (cm^2), ΔE_s is the change in the cell voltage during the charging (discharging) process, ΔE_t the change in voltage during resting to equilibrium, and L is the thickness of the electrode. Figure S33a (Supporting Information) shows that the diffusion coefficient of the HP-VO$_x$-50 electrode is about 10^{-9} to 10^{-11}, which is enhanced by an average of 1–2 orders of magnitude (Figure 4i) at different charging and discharging voltages when compared with P-VO$_x$-50 (Figure S33b, Supporting Information). This also demonstrates that the HP-VO$_x$-50 electrode exhibits fast electrochemical reaction kinetics during both charging and discharging.

Next, we assembled a HP-VO$_x$//Li interdigital microbattery using the HP-VO$_x$-50 electrode and lithium–copper composite tape. The electrochemical performance of the HP-VO$_x$//Li microbattery (MB) was evaluated, and the cyclic voltammetry (CV) results, shown in Figure 5a, maintain a similar profile to that of the individual electrode. Figure 5b presents the galvanostatic charge/discharge (GCD) curves of the HP-VO$_x$//Li MB at current densities ranging from 0.5 to 2.0 mA cm^{-2}, displaying a discharge plateau between 2.3 and 3.0 V, consistent with the CV results. At a current density of 0.5 mA cm^{-2}, the HP-VO$_x$//Li MB demonstrates an area capacity of 0.25 mAh cm^{-2}, with a capacity retention of 60% at 2.0 mA cm^{-2}. After 180 cycles, the capacity retention remains at 75%, as shown in Figure 5c. To evaluate the practical application potential of the HP-VO$_x$//Li MB, we powered an electronic timer continuously for more than 18 h, as shown in Figure 5d. This result highlights the effectiveness of our double-stacked encapsulation process. The simple

and cost-effective electrode preparation method, combined with the encapsulation strategy, presents a promising approach for future practical applications.
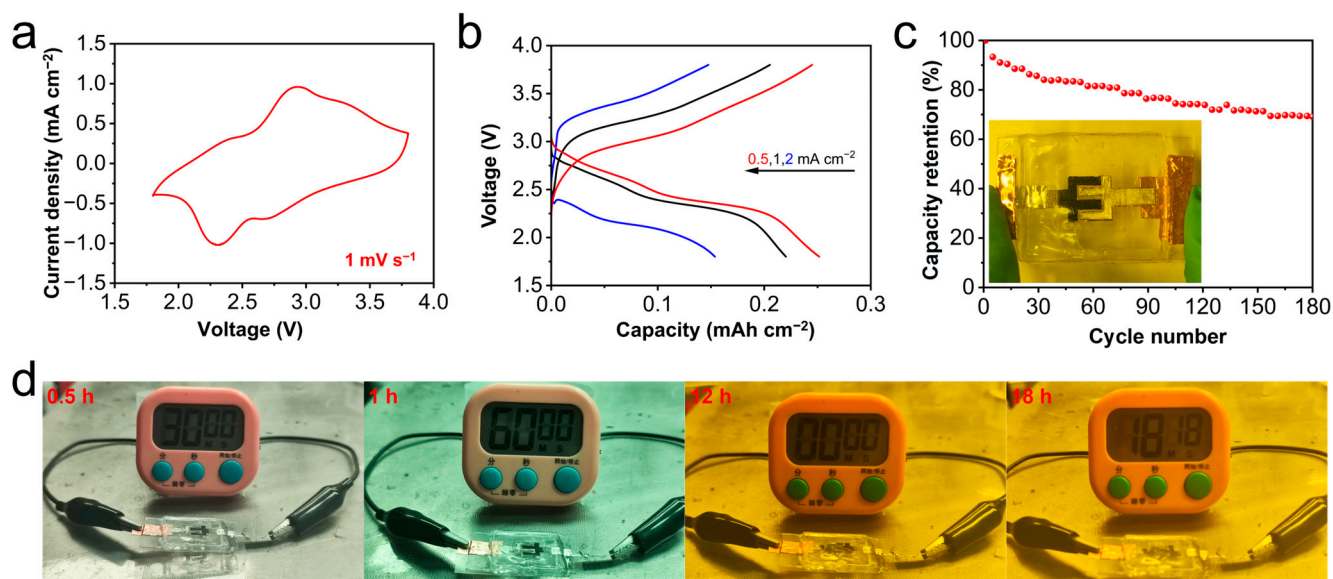

Figure 5. Schematic and performance diagram of a microbattery fabricated from a HP-VO$_x$ electrode. (**a**) CV curves of microbattery at 1 mV s^{-1}. (**b**) GCD curves of microbattery at different current densities. (**c**) Cycling performance of microbattery. (**d**) Application of microbattery to electronic clocks.

4. Conclusions

In conclusion, hierarchical porous current collectors were fabricated on commercial nickel foam using a simple, low-cost hydrogen templating method. Ultrathin α-VO$_x$ nanosheets were then conformally integrated onto the collectors using the same deposition method to create the hierarchical porous current electrodes. These electrodes exhibit high porosity, a dense network of active sites, and retain their porous structure even after the active material is loaded. The resulting electrode achieves a high energy density of 0.49 mAh cm^{-2} at 1 mA cm^{-2} and an ultrahigh power density of 410 mW cm^{-2} at 250 mA cm^{-2}. These remarkable performance characteristics are attributed to the dominance of capacitive behavior at the surface interface and the fast Li$^+$ diffusion rate ($\sim$10^{-9}–10^{-11} cm^2 s^{-1}), facilitated by the hierarchical porous structure and ultrathin α-VO$_x$ nanosheets (5–7 nm). Furthermore, a novel double-layer encapsulation method was employed to prevent electrolyte leakage and Li-metal electrode oxidation, significantly improving the microbattery's stability. This approach allowed the microbattery to cycle more than 180 times and power an electronic clock for over 18 h on a single charge.

hierarchical porous electrode; Figure S14: EDS mapping images of V and O elements of HP-VO$_x$-20; Figure S15: EDS mapping images of V and O elements of HP-VO$_x$-40; Figure S16: EDS mapping images of V and O elements of HP-VO$_x$-75; Figure S17: EDS mapping images of V and O elements of HP-VO$_x$-100; Figure S18: EDS mapping images of V and O elements of P-VO$_x$-50; Figure S19: AFM image of (a) hierarchical porous current collector and (b) HP-VO$_x$ electrode; Figure S20: Raman scattering spectra of HP-VO$_x$-50; Figure S21: GCD curves of HP-VO$_x$-20 electrode at various current densities; Figure S22: GCD curves of HP-VO$_x$-40 electrode at various current densities; Figure S23: GCD curves of HP-VO$_x$-75 electrode at various current densities; Figure S24: GCD curves of HP-VO$_x$-100 electrode at various current densities; Figure S25: GCD curves of P-VO$_x$-50 electrode at various current densities; Figure S26: XRD spectra of HP-VO$_x$-50 electrode after long cycling; Figure S27: SEM images of HP-VO$_x$-50 electrode after long cycling; Figure S28: EDS spectra of HP-VO$_x$-50 electrode after long cycling; Figure S29: The 3D plot of the contribution to the capacitive behavior of the HP-VO$_x$-50 electrode from 1 to 4 mV s^{-1} sweep rates; Figure S30: 3D EIS plots of P-VO$_x$-50 electrode at different temperatures; Figure S31: EIS curves at different temperatures for HP-VO$_x$-50 electrode. (a) 20 °C, (b) 30 °C, (c) 40 °C, (d) 50 °C, (e) 60 °C, (f) 70 °C and (g) 80 °C; Figure S32: EIS curves at different temperatures for P-VO$_x$-50 electrode. (a) 20 °C, (b) 30 °C, (c) 40 °C, (d) 50 °C, (e) 60 °C, (f) 70 °C and (g) 80 °C; Figure S33: GITT curves and Li$^+$ diffusion rate plots for (a) HP-VO$_x$-50 and (b) P-VO$_x$-50 electrode.

Author Contributions: Conceptualization, X.X.; methodology, X.C.; formal analysis, X.C., M.G. and J.L.; investigation, X.C. and M.G.; writing—original draft preparation, X.C.; writing—review and editing, W.Y. and X.X.; supervision, J.L.; funding acquisition, W.Y. All authors have read and agreed to the published version of the manuscript.

Data Availability Statement: The raw data supporting the conclusions of this article will be made available by the authors on request.

Conflicts of Interest: Author Xu Xu was employed by the company Zhongyu Feima New Material Technology Innovation Center (Zhengzhou) Co., Ltd. The remaining authors declare that the research was conducted in the absence of any commercial or financial relationships that could be construed as a potential conflict of interest.

References

1. Zhu, M.; Schmidt, O.G. Tiny Robots and Sensors Need Tiny Batteries—Here's How to Do It. *Nature* **2021**, *589*, 195–197. [CrossRef]
2. Zhu, J.; Ni, J.; Li, L. Harnessing In Situ Iodine Ionic Liquids for High Areal Capacity and Long Cycle Life Zn//I$_2$ Solid Microbatteries. *Adv. Funct. Mater.* **2024**, 2416799. [CrossRef]
3. Li, S.; Zhao, T.; Wang, H.; Wang, Z.; Zhang, M.; Shao, A.; Liu, J.; Wang, Z.; Ma, Y. High-Areal-Capacity/Power Lithium Metal Microbattery Configuration Based on the Mechanically Flexible, Ultra-Lightweight, Nanocellulose Framework. *Nano Res.* **2024**, *17*, 8155–8162. [CrossRef]
4. Choi, J.M.; Saroha, R.; Kim, J.S.; Jang, M.R.; Cho, J.S. Porous Nanofibers Comprising VN Nanodots and Densified N-Doped CNTs as Redox-Active Interlayers for Li–S Batteries. *J. Power Sources* **2023**, *559*, 232632. [CrossRef]
5. Liu, S.; Liu, W.; Zhao, Y.; Ye, Y.; Li, Y.; Liu, J. Filler-Integrated Composite Polymer Electrolyte for Solid-State Lithium Batteries. *Adv. Mater.* **2023**, *35*, 2110123. [CrossRef] [PubMed]
6. Li, Y.; Xiao, S.; Qiu, T.; Lang, X.; Tan, H.; Wang, Y.; Li, Y. Recent Advances on Energy Storage Microdevices: From Materials to Configurations. *Energy Storage Mater.* **2022**, *45*, 741–767. [CrossRef]
7. Peng, J.; Zhang, W.; Wang, S.; Huang, Y.; Wang, J.; Liu, H.; Dou, S.; Chou, S. The Emerging Electrochemical Activation Tactic for Aqueous Energy Storage: Fundamentals, Applications, and Future. *Adv. Funct. Mater.* **2022**, *32*, 2111720. [CrossRef]
8. Wang, X.; Wu, Z. Zinc Based Micro-electrochemical Energy Storage Devices: Present Status and Future Perspective. *EcoMat* **2020**, *2*, e12042. [CrossRef]
9. Jiang, M.; Hou, Z.; Ren, L.; Zhang, Y.; Wang, J.-G. Prussian Blue and Its Analogues for Aqueous Energy Storage: From Fundamentals to Advanced Devices. *Energy Storage Mater.* **2022**, *50*, 618. [CrossRef]
10. Zhang, X.; Hu, L.; Zhou, K.; Zhang, L.; Zeng, X.; Shi, Y.; Cai, W.; Wu, J.; Lin, Y. Fully Printed and Sweat-Activated Micro-Batteries with Lattice-Match Zn/MoS$_2$ Anode for Long-Duration Wearables. *Adv. Mater.* **2024**, *36*, 2412844. [CrossRef] [PubMed]

11. Li, X.; Jin, X.; Wang, Y.; Zhang, X.; Li, D.; Wang, J.; Yuan, M.; Liu, J.; Zhao, Y. All-Direct Laser Patterning Zinc-Based Microbatteries. *Adv. Funct. Mater.* **2024**, *34*, 2314060. [CrossRef]

12. Jin, X.; Song, L.; Dai, C.; Xiao, Y.; Han, Y.; Li, X.; Wang, Y.; Zhang, J.; Zhao, Y.; Zhang, Z.; et al. A Flexible Aqueous Zinc–Iodine Microbattery with Unprecedented Energy Density. *Adv. Mater.* **2022**, *34*, 2109450. [CrossRef]

13. Yang, W.; Xu, L.; Luo, W.; Huang, M.; Fu, K.; Song, R.; Han, C.; Tu, R.; Shi, J.; Mai, L. Rechargeable Zinc-Ammonium Hybrid Microbattery with Ultrahigh Energy and Power Density. *Matter* **2023**, *6*, 3006–3020. [CrossRef]

14. Tang, M.; Dong, S.; Wang, J.; Cheng, L.; Zhu, Q.; Li, Y.; Yang, X.; Guo, L.; Wang, H. Low-Temperature Anode-Free Potassium Metal Batteries. *Nat. Commun.* **2023**, *14*, 6006. [CrossRef] [PubMed]

15. Liang, P.; Sun, H.; Huang, C.; Zhu, G.; Tai, H.; Li, J.; Wang, F.; Wang, Y.; Huang, C.; Jiang, S.; et al. A Nonflammable High-Voltage 4.7 V Anode-Free Lithium Battery. *Adv. Mater.* **2022**, *34*, 2207361. [CrossRef] [PubMed]

16. Ma, J.; Zheng, S.; Chi, L.; Liu, Y.; Zhang, Y.; Wang, K.; Wu, Z. 3D Printing Flexible Sodium-Ion Microbatteries with Ultrahigh Areal Capacity and Robust Rate Capability. *Adv. Mater.* **2022**, *34*, 2205569. [CrossRef]

17. Lu, Y.; Wang, Z.; Li, M.; Li, Z.; Hu, X.; Xu, Q.; Wang, Y.; Liu, H.; Wang, Y. 3D Printed Flexible Zinc Ion Micro-Batteries with High Areal Capacity Toward Practical Application. *Adv. Funct. Mater.* **2024**, *34*, 2310966. [CrossRef]

18. Zhang, Y.; Wang, Y.; Zhao, W.; Zuo, P.; Tong, Y.; Yin, G.; Zhu, T.; Lou, S. Delocalized Electronic Engineering of $TiNb_2O_7$ Enables Low Temperature Capability for High-Areal-Capacity Lithium-Ion Batteries. *Nat. Commun.* **2024**, *15*, 6299. [CrossRef] [PubMed]

19. Yang, J.; Li, Y.; Mijailovic, A.; Wang, G.; Xiong, J.; Mathew, K.; Lu, W.; Sheldon, B.W.; Wu, Q. Gradient Porosity Electrodes for Fast Charging Lithium-Ion Batteries. *J. Mater. Chem. A* **2022**, *10*, 12114–12124. [CrossRef]

20. Zhang, X.; Hui, Z.; King, S.T.; Wu, J.; Ju, Z.; Takeuchi, K.J.; Marschilok, A.C.; West, A.C.; Takeuchi, E.S.; Wang, L.; et al. Gradient Architecture Design in Scalable Porous Battery Electrodes. *Nano Lett.* **2022**, *22*, 2521–2528. [CrossRef]

21. Liu, X.; Liu, Y.; Zhang, Q.; Zhou, S.; Li, X.; Yi, B.; Liu, Y.; Liu, X.; Ding, Y. Integrating Aperiodic 3D Porous Electrodes into 3D Batteries through Spray-Deposited Polymer Electrolytes. *Adv. Energy Mater.* **2024**, *14*, 2401330. [CrossRef]

22. Sun, P.; Li, X.; Shao, J.; Braun, P.V. High-Performance Packaged 3D Lithium-Ion Microbatteries Fabricated Using Imprint Lithography. *Adv. Mater.* **2021**, *33*, 2006229. [CrossRef]

23. Hur, J.I.; Smith, L.C.; Dunn, B. High Areal Energy Density 3D Lithium-Ion Microbatteries. *Joule* **2018**, *2*, 1187–1201. [CrossRef]

24. Hao, Z.; Xu, L.; Liu, Q.; Yang, W.; Liao, X.; Meng, J.; Hong, X.; He, L.; Mai, L. On-Chip Ni–Zn Microbattery Based on Hierarchical Ordered Porous Ni@Ni(OH)$_2$ Microelectrode with Ultrafast Ion and Electron Transport Kinetics. *Adv. Funct. Mater.* **2019**, *29*, 1808470. [CrossRef]

25. Lee, S.A.; Yang, J.W.; Choi, S.; Jang, H.W. Nanoscale Electrodeposition: Dimension Control and 3D Conformality. *Exploration* **2021**, *1*, 20210012. [CrossRef] [PubMed]

26. Yang, W.; Xu, L.; Luo, W.; Li, M.; Hu, P.; Dai, Y.; Ye, F.; Han, C.; Zhou, M.; Tu, R.; et al. 3D Macroporous Frame Based Microbattery with Ultrahigh Capacity, Energy Density, and Integrability. *Adv. Energy Mater.* **2023**, *13*, 2300574. [CrossRef]

27. Li, Z.; Xu, Y.; Wu, L.; Dou, H.; Zhang, X. Microstructural Engineering of Hydrated Vanadium Pentoxide for Boosted Zinc Ion Thermoelectrochemical Cells. *J. Mater. Chem. A* **2022**, *10*, 21446–21455. [CrossRef]

28. Hevia, S.A. High Performance of V_2O_5 Thin Film Electrodes for Lithium-Ion Intercalation. *Appl. Surf. Sci.* **2022**, *576*, 151710. [CrossRef]

29. Ning, H.; Pikul, J.H.; Zhang, R.; Li, X.; Xu, S.; Wang, J.; Rogers, J.A.; King, W.P.; Braun, P.V. Holographic Patterning of High-Performance on-Chip 3D Lithium-Ion Microbatteries. *Proc. Natl. Acad. Sci. USA* **2015**, *112*, 6573–6578. [CrossRef]

30. Kotobuki, M.; Suzuki, Y.; Munakata, H.; Kanamura, K.; Sato, Y.; Yamamoto, K.; Yoshida, T. Effect of Sol Composition on Solid Electrode/Solid Electrolyte Interface for All-Solid-State Lithium Ion Battery. *Electrochim. Acta* **2011**, *56*, 1023–1029. [CrossRef]

31. Pikul, J.H.; Gang Zhang, H.; Cho, J.; Braun, P.V.; King, W.P. High-Power Lithium Ion Microbatteries from Interdigitated Three-Dimensional Bicontinuous Nanoporous Electrodes. *Nat. Commun.* **2013**, *4*, 1732. [CrossRef]

32. Yoshima, K.; Munakata, H.; Kanamura, K. Fabrication of Micro Lithium-Ion Battery with 3D Anode and 3D Cathode by Using Polymer Wall. *J. Power Sources* **2012**, *208*, 404–408. [CrossRef]

33. Sun, K.; Wei, T.; Ahn, B.Y.; Seo, J.Y.; Dillon, S.J.; Lewis, J.A. 3D Printing of Interdigitated Li-Ion Microbattery Architectures. *Adv. Mater.* **2013**, *25*, 4539–4543. [CrossRef] [PubMed]

34. Acharya, J.; Ko, T.H.; Seong, J.-G.; Seo, M.-K.; Khil, M.-S.; Kim, H.-Y.; Kim, B.-S. Hybrid Electrodes Based on Zn–Ni–Co Ternary Oxide Nanowires and Nanosheets for Ultra-High-Rate Asymmetric Supercapacitors. *ACS Appl. Nano Mater.* **2020**, *3*, 8679–8690. [CrossRef]

35. Brezesinski, T.; Wang, J.; Tolbert, S.H.; Dunn, B. Ordered Mesoporous α-MoO$_3$ with Iso-Oriented Nanocrystalline Walls for Thin-Film Pseudocapacitors. *Nat. Mater* **2010**, *9*, 146–151. [CrossRef] [PubMed]

36.	Tu, S.; Zhang, B.; Zhang, Y.; Chen, Z.; Wang, X.; Zhan, R.; Ou, Y.; Wang, W.; Liu, X.; Duan, X.; et al. Fast-Charging Capability of Graphite-Based Lithium-Ion Batteries Enabled by Li$_3$P-Based Crystalline Solid–Electrolyte Interphase. *Nat. Energy* **2023**, *8*, 1365–1374. [CrossRef]

37.	Gong, S.; Sun, K.; Cao, N.; Chao, D.; Jia, X.; Wang, C. Potassium Phthalimide Doped with Delta-Site Structures to Construct Ultra-Long Cycle Life Aqueous Zn-Polymer Batteries. *Adv. Funct. Mater.* **2024**, *34*, 2409805. [CrossRef]